Langtaosha (LTS) Preprint doi: https://doi.org/10.65215/LTSpreprints.2026.11.23.000399. This version posted November 23, 2026. The copyright holder for this preprint (which was not certified by peer review) is the author/funder. Creative Commons license: CC Attribution-NonCommercial-NoDerivatives 4.0 https://creativecommons.org/licenses/by-nc-nd/4.0

Mechanistic insights into allosteric PKR activation guide design of a clinical-stage allosteric agonist

Haiyun Ma[1,2], Quanwei Yu[1], Ling Zhang[3], Xiao Hu[3], Zao Wang[3], Jing Wang[3], Jun Tang[3], Zhaoming Su[1,*]

[1]Center of Infectious Diseases, State Key Laboratory of Biotherapy and Biosafety Laboratory, Institute of Infection and Infectious Diseases, West China Hospital, Sichuan University, Chengdu 610044, China.

[2]Tianfu Jincheng Laboratory, Chengdu, 610093, China.

[3]ScinnoHub Pharmaceutical Co., Ltd, No. 263 Hexiang Third Street, Shuangliu District, Chengdu, 610000, China

*Correspondence should be addressed to Z.S. (zsu@wchscu.cn).

Abstract

Pyruvate kinase R (PKR) activation is a therapeutic strategy for pyruvate kinase deficiency, sickle cell disease and thalassaemia, but how FDA-approved mitapivat and clinical-stage etavopivat recognize and regulate PKR remains elusive. In this study, we use cryo-EM to elucidate their distinct allosteric recognition modes. Mitapivat adopts single- and dual-ligand states in the intersubunit allosteric pockets, whereas etavopivat inserts in between two phenylalanines (F69s) through π-stacking and hydrogen bond interactions. The ligand-bound structures reveal an ordered N-terminus containing F69, which is too flexible to be resolved in the apo-PKR, suggesting a mechanism of ligand-induced local stabilization and conformational selection. Pharmacophore optimization guided by the etavopivat mode of action (MOA) yields SNH-119014, with AC_{50} values of 7.35 nM in recombinant PKR and 24.2-31.7 nM in erythrocytes from two donors, comparable to the approved mitapivat and the clinical-stage etavopivat in potency but with an approximately two-fold higher maximal PKR activation than etavopivat. Cryo-EM structures further elucidate the MOAs of SNH-119014 and BT-119106, sharing analogous recognition patterns with etavopivat. These results provide mechanistic insights into allosteric PKR activation of approved drugs, and facilitate design of new allosteric agonists with improved PKR activation for clinical applications.

Keywords

Pyruvate kinase R activation; mitapivat; etavopivat; SNH-119014; allosteric agonist; cryo-EM

Introduction

Langtaosha (LTS) Preprint doi: https://doi.org/10.65215/LTSpreprints.2026.11.23.000399. This version posted November 23, 2026. The copyright holder for this preprint (which was not certified by peer review) is the author/funder. Creative Commons license: CC Attribution-NonCommercial-NoDerivatives 4.0 https://creativecommons.org/licenses/by-nc-nd/4.0

Pyruvate kinase (PK) is a key rate-limiting enzyme in glycolysis that catalyses the final irreversible step, converting phosphoenolpyruvate (PEP) and adenosine diphosphate (ADP) into pyruvate and adenosine triphosphate (ATP). PK activity is tightly controlled by allosteric regulation, including homotropic activation by its substrate PEP and heterotropic activation by the glycolytic intermediate fructose 1,6-bisphosphate (FBP). Mammals express four tissue-specific PK isoforms: the L isoform (PKL) in the liver, the R isoform (PKR) in erythrocytes[1], the M1 isoform (PKM1) predominantly in muscle and brain, and the M2 isoform (PKM2) highly expressed in fetal and proliferating cells including tumour cells[2]. Because mature erythrocytes lack mitochondria and depend heavily on glycolysis for energy production, reduced PKR activity disrupts cellular energy homeostasis, membrane integrity and deformability[3,4]. It also promotes the accumulation of the upstream metabolite 2,3-diphosphoglycerate (2,3-DPG), thereby decreasing the oxygen affinity of haemoglobin[3]. Pathogenic variants in the *PKLR* gene coding PKL and PKR cause pyruvate kinase deficiency, whereas acquired reductions in PKR activity or stability may also exacerbate the metabolic abnormalities associated with sickle cell disease and thalassaemia[1,5,6]**.** Pharmacological activation of PKR may therefore improve erythrocyte energy metabolism in PK deficiency and haemoglobinopathies and, in sickle cell disease, may also reduce metabolic conditions that favour haemoglobin S polymerization[5,7].

Mitapivat (AG-348) became the first PKR agonist approved for adults with pyruvate kinase deficiency, thereby validating PKR activation as a therapeutic strategy[8–10]. The clinical-stage compounds etavopivat (FT-4202) and tebapivat (AG-946) subsequently broadened the chemical diversity of interfacial PKR agonists[11–13]**.** These compounds bind to an allosteric pocket formed at the PKR dimer interface, which is spatially separated from the catalytic centre[14,15]. However, mechanistic understanding of their precise modes of action (MOAs) has lagged behind their clinical development. The earlier PKR-mitapivat crystal structure did not fully resolve the ligand electron density and modelled one ligand in one interfacial pocket but two in the other[14], whereas a more recent PKL-mitapivat crystal structure and its isothermal titration calorimetry both indicated one ligand per pocket[16]. These discrepancies left the mitapivat binding stoichiometry and MOA unresolved.

To address these questions, we combined single-particle cryo-electron microscopy (cryo-EM), recombinant enzyme assays, ex vivo erythrocyte functional assays, molecular dynamics (MD) simulations and structure-guided pharmacophore optimization to define how the interfacial allosteric pocket of human PKR recognizes chemically distinct agonists. We determined the ligand-free (apo) structure of the full-length human PKR tetramer, and complexes with the approved drug mitapivat and the clinical-stage agonist etavopivat. These structures elucidate the dynamic occupancy of mitapivat and the MOA of etavopivat, in which a single molecule inserts between the F69 side chains of two adjacent protomers through π-stacking, while its hydroxyacyl terminus forms a hydrogen bond to the Y433 backbone within a hydrophobic environment formed by L70, L73, V432 and L437. Comparisons between apo-PKR and the ligand-bound PKR

Langtaosha (LTS) Preprint doi: https://doi.org/10.65215/LTSpreprints.2026.11.23.000399. This version posted November 23, 2026. The copyright holder for this preprint (which was not certified by peer review) is the author/funder. Creative Commons license: CC Attribution-NonCommercial-NoDerivatives 4.0 https://creativecommons.org/licenses/by-nc-nd/4.0

complexes suggest a working model of allosteric agonists inducing local stabilization of allosteric pockets and intersubunit contacts through conformational selection. Guided by the etavopivat MOA, we optimized a series of PKR agonists with recombinant AC_{50} values improving from 215 nM to 6.70 nM, yielding a clinical candidate SNH-119014 that matches mitapivat and etavopivat in potency, while approximately doubling the maximal PKR activation of etavopivat. SNH-119014 has been recently registered for phase 2 clinical trial[17]. Cryo-EM structures of PKR bound to SNH-119014 and the optimization intermediate BT-119106 reveal MOAs analogous to that of etavopivat. Together, these findings reveal the conformational plasticity and ligand-induced recognition of the PKR interfacial allosteric binding site, and facilitate development of next-generation PKR agonists for hereditary anaemias.

Results

Mitapivat adopts single- and dual-ligand states occupying the PKR interfacial pocket

Full-length human PKR was expressed in Escherichia coli and purified by size-exclusion chromatography (Extended Data Fig. 1a). Negative-stain and cryo-EM showed the expected tetrameric architecture and well-dispersed particles, respectively (Extended Data Fig. 1b,c). Each protomer comprises an N-terminal domain and the A, B and C domains; four protomers assemble through two A-A′ and two C-C′ interfaces (Fig. 1a). Each A-A′ interface forms an allosteric pocket spatially distinct from the catalytic and endogenous allosteric-effector sites, yielding two C2 symmetric interfacial pockets per tetramer (Fig. 1a). We next prepared a complex of PKR with mitapivat (Fig. 1b), the only FDA-approved PKR agonist, and determined its cryo-EM structure to elucidate the ligand recognition mechanism (Fig. 1c).

The PKR-mitapivat reconstruction reached 2.74 Å resolution with C1 symmetry (Extended Data Fig. 1d), and revealed density consistent with two mitapivat molecules in one interfacial pocket (Fig. 1c). Applying C2 symmetry along the C-C′ interface axis improved the global resolution to 2.57 Å and clarified the density of two head-to-tail mitapivat molecules in both A-A′ interfacial pockets (Fig. 1c and Extended Data Figs. 1d and 2a). C2 symmetry expansion of 767,192 particles, followed by subtraction and focused three-dimensional (3D) classification yielded six classes (Extended Data Fig. 2a), among which three classes showed explicit ligand densities and were refined to 2.92-2,93 Å resolutions (Extended Data Fig. 2b-d). These include one dual-ligand state and two single-ligand states with the mitapivat in alternative binding poses (Fig. 1c).

The mitapivat molecules in all three states occupy the same A-A′ interfacial pockets formed by F69, L70, L73, I357, L396, A431 and V432 from both protomers, with D397 and the neighboring polar residues at its solvent-exposed boundary. In every state the quinoline ring of mitapivat packs edge-to-face against F69 of the opposing protomer, and its sulfonamide forms hydrogen bonds to the L396 and Y433 backbone. In the dual-ligand state, the two mitapivat molecules pack head-to-

Langtaosha (LTS) Preprint doi: https://doi.org/10.65215/LTSpreprints.2026.11.23.000399. This version posted November 23, 2026. The copyright holder for this preprint (which was not certified by peer review) is the author/funder. Creative Commons license: CC Attribution-NonCommercial-NoDerivatives 4.0 https://creativecommons.org/licenses/by-nc-nd/4.0

tail around the A-A′ interface axis, each contacting the F69 of the opposite protomer and interacting with L396 and D397 through at least four ordered waters (Fig. 1d). In both single-ligand states, each mitapivat molecule occupies half of the A-A′ interfacial pocket, contacting K354, L396, D397 and Y433 directly or through ordered waters (Fig. 1e). Previous crystal structure of the mitapivat-bound PKL showed ligand-binding pose resembling one of our single-ligand states (Fig. 1f)[16], validating our single-ligand states separated from C2 symmetry expansion and focused classification. Our dual-ligand state also reconciles a previous mitapivat-bound PKR crystal structure with electron densities suggesting two mitapivat molecules bound in the A-A′ interfacial pocket [14,16].

To validate both single- and dual-mitapivat binding modes, we ran 1 μs MD simulations of apo-PKR and of PKR carrying one or two mitapivat molecules in each A-A′ pocket (Fig. 1g,h). Backbone RMSD values of the protomer residues were higher in both ligand-bound systems than that in the apo-PKR (4.43 and 4.73 Å versus 3.16 Å), whereas RMSD values of the 29 residues forming the pocket were lower than that in the apo-PKR (1.73 and 1.65 Å versus 1.96 Å). Both the single- and dual-ligand binding modes therefore hold the pocket steady while the rest of PKR continues to move, and each binding mode remained stable throughout its trajectory.

Etavopivat adopts a single-ligand cross-interface MOA

Etavopivat (FT-4202) is an orally available next-generation PKR agonist that is chemically unrelated to mitapivat and is under phase 2/3 evaluation for sickle cell disease and thalassaemia[11,12] (Fig. 2a), however, its binding mode has been inferred only from a closely related analogue[15]. We therefore determined a 2.81 Å cryo-EM structure of the PKR-etavopivat complex (Fig. 2b and Extended Data Fig. 3). In contrast to mitapivat, a single etavopivat molecule was explicitly resolved occupying each of the two A-A′ pockets, giving two ligands per tetramer (Fig. 2b). The pocket surface around the ligand is neutral to weakly negative (Fig. 2c). Etavopivat spans the A-A′ interface and inserts between the F69 side chains of the two protomers, forming π-stacking contacts with both in a hydrophobic environment consisting of L70, L73, V432 and L437 (Fig. 2d). Adjacent to the fused bicyclic diamine core, the hydroxyl and sulfonyl groups form hydrogen bonds with the backbones of Y433 and L437 (Fig. 2d).

Tebapivat (AG-946) is a second next-generation PKR agonist, developed by structure-based design and currently in phase 2 trials for sickle cell disease and lower-risk myelodysplastic syndromes[13]. Superposition with PKR-bound tebapivat shows a similar binding mode despite their distinct chemical cores and local contacts (Fig. 2e)[13]. Comparison with the mitapivat structures reveals that the next-generation agonists, etavopivat and tebapivat, contact F69 residues from both protomers simultaneously through sandwiched π-stackings, whereas the single- and dual-binding mitapivat molecules only surround the A-A′ pocket through multiple weaker interactions (Fig. 2f).

Langtaosha (LTS) Preprint doi: https://doi.org/10.65215/LTSpreprints.2026.11.23.000399. This version posted November 23, 2026. The copyright holder for this preprint (which was not certified by peer review) is the author/funder. Creative Commons license: CC Attribution-NonCommercial-NoDerivatives 4.0 https://creativecommons.org/licenses/by-nc-nd/4.0

Clinical agonist binding to the pre-existing allosteric pocket facilitates ordering of surrounding regions

To define what agonist binding changes, we compared both complexes with apo-PKR. The apo-PKR reconstruction reached 2.34 Å resolution, and focused classification on the B domain recovered a more complete configuration at 2.48 Å (Extended Data Fig. 4). The tetramer is intact and the allosteric pockets are already formed at both A-A′ interfaces without ligand-binding (Fig. 3a). However, the N-terminal region surrounding the pocket is poorly ordered, with residues 1-64 unresolved and the F69-containing segment (residues 65-84) discontinuous (Fig. 3a). Three-dimensional variability analysis (3DVA) of the apo-PKR resolved a continuum of motions in this N-terminal segment (Extended Data Fig. 4 and Supplementary Movie 1), indicating high flexibility before ligand binding. In the mitapivat- and etavopivat-bound structures, agonist binding has enforced the regions around the A-A′ pockets to become ordered and better resolved (Fig. 3a), although the B domain remained heterogeneous.

These results suggest a working model that combines ligand-induced local stabilization with conformational selection (Fig. 3b) [18–21]. An agonist selects a compatible pocket conformation from those that apo-PKR already samples, and then stabilizes the surrounding regions. Mitapivat and etavopivat differ in ligand stoichiometry and MOA, yet both occupy the same pocket and order the same regions.

Pharmacophore optimization yields a chemically distinct series of PKR agonists

The PKR-etavopivat structure provided a geometric template for agonist design. A single etavopivat molecule spans the A-A′ interfacial pocket and directs its hydroxyacyl and sulfonyl termini toward the two protomers, so that the separation between the two substituted nitrogen atoms of its central core determines how both termini are presented (Fig. 4a). In etavopivat this core is an unsaturated fused bicyclic diamine (Core Scaffold 1) with a nitrogen-nitrogen distance of 4.23 Å (Fig. 4a,b). Guided by previously reported alkene-linked azacyclic bioisosteres[22], we replaced it with two azetidine rings joined by an exocyclic carbon-carbon double bond (Core Scaffold 2), widening this distance to 5.45 Å (Fig. 4a,b).

Transplanting both etavopivat termini onto Core Scaffold 2 yielded BT-119014, whose half-maximal activation concentration (AC_{50}) against recombinant PKR rose from 6.26 nM for etavopivat to 215 nM, a 34-fold loss of potency (Fig. 4b,c). Redesigning the sulfonyl-linked terminus restored the AC_{50} to 6.70 nM in BT-119067 (Fig. 4b,c), showing that Core Scaffold 2 supports low-nanomolar PKR activation once its termini are matched to the widened core.

Further optimization of both termini yielded BT-119106, combining an unsubstituted phenyl hydroxyacyl terminus with a 4-cyanophenylsulfonyl terminus, and SNH-119014, combining a 2,4-

Langtaosha (LTS) Preprint doi: https://doi.org/10.65215/LTSpreprints.2026.11.23.000399. This version posted November 23, 2026. The copyright holder for this preprint (which was not certified by peer review) is the author/funder. Creative Commons license: CC Attribution-NonCommercial-NoDerivatives 4.0 https://creativecommons.org/licenses/by-nc-nd/4.0

difluorophenyl hydroxyacyl terminus with a pyridin-2-ylsulfonyl terminus (Fig. 4b). Against recombinant PKR, mitapivat, etavopivat, BT-119067 and SNH-119014 gave AC_{50} values of 6.52, 6.26, 6.70 and 7.35 nM, whereas BT-119106 and BT-119014 gave 95.1 and 215 nM (Fig. 4c), placing SNH-119014 12.9-fold above the closely related BT-119106. Potency and maximal response did not track together across the series: SNH-119014 and etavopivat reached similar AC_{50} values but response plateaus of approximately 340% and 170% of the dimethyl sulfoxide (DMSO) control, respectively (Fig. 4c).

We next measured PK activity in lysates of erythrocytes from one healthy male and one healthy female donor after 4 h of compound exposure (Fig. 4d,e). AC_{50} values for the male and female samples were 28.3 and 17.1 nM for mitapivat, 32.3 and 29.9 nM for etavopivat, 20.3 and 16.5 nM for BT-119067, 31.7 and 24.2 nM for SNH-119014, 49.5 and 42.8 nM for BT-119106, and 68.8 and 112 nM for BT-119014 (Fig. 4d,e). SNH-119014 therefore retained potency comparable to mitapivat and etavopivat in intact erythrocytes, whereas its 12.9-fold advantage over BT-119106 narrowed to 1.6-fold and 1.8-fold.

SNH-119014 also reached higher response plateaus than etavopivat in both donors, approximately 138% and 140% of the DMSO control against 122% and 118% (Fig. 4d,e). Terminal-group optimization therefore recovered the potency lost to core replacement and, in addition, yielded an agonist that activates PKR to a higher maximal level than either clinical compound. We next used the 12.9-fold potency difference between BT-119106 and SNH-119014 to test whether this gain arises within the etavopivat MOA.

Optimized agonists retain the etavopivat cross-interface MOA and differ only at their termini

We determined cryo-EM structures of PKR bound to BT-119106 and SNH-119014 at 2.87 Å and 2.77 Å resolution, respectively (Extended Data Figs. 5 and 6). In both complexes a single ligand occupied each A-A′ interfacial pocket and spanned the two protomers (Fig. 5a,d), and Core Scaffold 2 adopted the same conformation, with nitrogen–nitrogen distances of 5.41 Å in BT-119106 and 5.46 Å in SNH-119014 (Fig. 5a,d). Both optimized agonists therefore retain the etavopivat MOA, without engaging an alternative site or adopting the paired occupancy of mitapivat.

The two agonists also share the same contacts across the A-A′ interface (Fig. 5b,c,e,f). In both, the hydroxyacyl terminus hydrogen bonds to the Y433 backbone, Core Scaffold 2 is accommodated by L70, L73, V432, Q436 and L437, and the aromatic groups at both ends pack edge-to-face against the F69 side chains of the two protomers (Fig. 5c,f). The differences are confined to the termini. The 4-cyanophenylsulfonyl terminus of BT-119106 extends toward N361, where its nitrile makes only limited polar contact (Fig. 5c), whereas the pyridin-2-ylsulfonyl terminus of SNH-

Langtaosha (LTS) Preprint doi: https://doi.org/10.65215/LTSpreprints.2026.11.23.000399. This version posted November 23, 2026. The copyright holder for this preprint (which was not certified by peer review) is the author/funder. Creative Commons license: CC Attribution-NonCommercial-NoDerivatives 4.0 https://creativecommons.org/licenses/by-nc-nd/4.0

119014 directs its ring nitrogen toward the E440-containing polar surface (Fig. 5f). The 2,4-difluorophenyl group of SNH-119014 fills the same F69-adjacent hydrophobic subpocket as the unsubstituted phenyl ring of BT-119106, but packs against it more closely (Fig. 5c,f).

The 12.9-fold potency difference between BT-119106 and SNH-119014 therefore arises within an unchanged MOA, from the polarity and packing of the two termini rather than from the binding site, the ligand stoichiometry or the core conformation. Because the two agonists differ at both termini, the individual contributions of the pyridin-2-yl nitrogen and the 2,4-difluoro substitution await separate measurement.

Discussion

Allosteric PKR agonists have reached the clinic ahead of a mechanistic description of how they activate the enzyme. Our structures provide that description for the approved drug and for a next-generation agonist, and show that one interfacial pocket supports more than one MOA. The PKR tetramer is essentially unchanged across apo-PKR and all four agonist complexes, yet the same A-A′ pocket accommodates either two mitapivat molecules that surround the interface, or a single etavopivat-type molecule that inserts into it.

Our mitapivat structures reconcile two conflicting crystallographic reports. The original PKR structure modelled one mitapivat molecule in one pocket and two in the other, whereas the later PKL structure and its isothermal titration calorimetry both indicated one ligand per pocket[14,16]. Focused classification of a single cryo-EM dataset resolved one dual-ligand and two single-ligand states within the same sample, so the two reports describe states that coexist, and MD simulations confirmed that both remain stable over 1 μs. Resolving an agonist that occupies an allosteric site in more than one way therefore requires cryo-EM heterogeneity analysis, and how these states are populated in solution remains to be measured.

Etavopivat and tebapivat engage the same pocket through a different MOA. A single molecule inserts between the two F69 side chains and forms sandwiched π-stacking with both protomers simultaneously, whereas mitapivat contacts one F69 at a time through edge-to-face packing and surrounds the interface through multiple weaker interactions. Bilateral single-molecule recognition is thus the chemical feature that separates the next-generation agonists from mitapivat, and the feature that can be transferred to a new scaffold.

Agonist binding does not create the pocket. The A-A′ pocket and its intersubunit contacts are already present in apo-PKR, and what binding adds is ordering of the mobile N-terminal region that carries F69. Chemically distinct agonists converge on one pre-existing pocket while organizing its surroundings differently, consistent with a coupled model of ligand-induced local stabilization and conformational selection[18–21].

Langtaosha (LTS) Preprint doi: https://doi.org/10.65215/LTSpreprints.2026.11.23.000399. This version posted November 23, 2026. The copyright holder for this preprint (which was not certified by peer review) is the author/funder. Creative Commons license: CC Attribution-NonCommercial-NoDerivatives 4.0 https://creativecommons.org/licenses/by-nc-nd/4.0

Widening the core from 4.2 to 5.4 Å resulted in 34-fold loss in potency, and redesigning the termini recovered it, showing that a new core is tolerated only when it still presents both termini to their respective protomers. The BT-119106 and SNH-119014 structures closed this design cycle: both retain the single-ligand cross-interface MOA with indistinguishable core conformations, and their 12.9-fold potency difference maps entirely onto the termini contacting N361, E440 and F69. Once the interface-spanning geometry is fixed, terminal complementarity is critical for optimization.

SNH-119014 separates potency from maximal response. It matches mitapivat and etavopivat in AC_{50} against both recombinant PKR and intact erythrocytes, but raises PKR activity to approximately twice the level reached with etavopivat in both assays. Because erythrocyte ATP production scales with the PK activity attained rather than with the agonist concentration required, maximal response may be the more consequential parameter in hereditary anaemias. SNH-119014 has been registered for phase 2 evaluation in adults with non-transfusion-dependent thalassaemia[17], which will test this directly.

In conclusion, the A-A′ interfacial pocket of PKR is a pre-existing allosteric site that accommodates chemically distinct agonists through distinct MOAs, and these MOAs can be read out structurally and transferred to new scaffolds. Matching the scaffold span to the intersubunit geometry, preserving bilateral F69 recognition and optimizing terminal complementarity together define a design route to next-generation PKR agonists, which here delivered SNH-119014 into clinical evaluation for hereditary anaemias.

Methods

Plasmid construction

The codon-optimized coding sequence of human wild-type PKR (UniProt P30613) was cloned into a modified pET28a vector carrying an N-terminal 10×His-SUMO tag, and the final construct pET28a-10His-SUMO-PKR was verified by DNA sequencing.

Expression and purification of PKR

The pET28a-10His-SUMO-PKR plasmid was transformed into *Escherichia coli* BL21(DE3). Single colonies were grown in lysogeny broth containing 50 μg/mL kanamycin at 37 °C with continuous shaking at 220 r.p.m. When the culture reached an OD_{600} of 0.6-0.8, expression was induced with 0.5 mM isopropyl β-D-1-thiogalactopyranoside (IPTG) and continued at 18 °C for 16 h. Cells were then harvested by centrifugation at 8,000 g and 4 °C for 15 min.

The cell pellet was resuspended in binding buffer containing 25 mM Tris-HCl (pH 7.8), 500 mM NaCl and 5% glycerol, freshly supplemented with 1 mM phenylmethylsulfonyl fluoride, and lysed at 100 MPa in a high-pressure homogenizer. The lysate was clarified by centrifugation at 18,000 g and 4 °C for 40 min, and the supernatant was loaded onto a HisTrap HP column (GE Healthcare)

Langtaosha (LTS) Preprint doi: https://doi.org/10.65215/LTSpreprints.2026.11.23.000399. This version posted November 23, 2026. The copyright holder for this preprint (which was not certified by peer review) is the author/funder. Creative Commons license: CC Attribution-NonCommercial-NoDerivatives 4.0 https://creativecommons.org/licenses/by-nc-nd/4.0

equilibrated with binding buffer containing 10 mM imidazole. The column was washed stepwise with the same buffer adjusted to 50 and 80 mM imidazole, and His-SUMO-PKR was eluted with elution buffer containing 25 mM Tris-HCl (pH 7.8), 300 mM NaCl, 300 mM imidazole and 5% glycerol. The eluate was exchanged into cleavage buffer containing 25 mM Tris-HCl (pH 7.8) and 150 mM NaCl, and incubated with ULP1 protease overnight at 4 °C to remove the His-SUMO tag. The cleavage mixture was reapplied to a HisTrap HP column and tag-free PKR was collected in the flow-through, concentrated on an ultrafiltration device (Millipore) and further purified by size-exclusion chromatography on a Superdex 200 Increase 10/300 GL column (GE Healthcare) equilibrated with cleavage buffer. Peak fractions were assessed by SDS-PAGE, pooled and used directly for cryo-EM sample preparation, or aliquoted and stored at -80 °C.

Negative staining electron microscopy

Purified PKR at 4 mg/mL was diluted in Buffer G to 0.10, 0.05 and 0.01 mg/mL. Aliquots (3.5 µl) were applied to glow-discharged (40 s) 300-mesh continuous-carbon copper grids (Quantifoil) and incubated for 60 s. Each grid was washed twice with fresh drops of 0.75% (w/v) uranyl acetate and stained with a third drop for 50 s. Excess stain was blotted away, and the grids were air-dried. Micrographs were collected on a JEOL JEM-1400 transmission electron microscope operated at 120 kV using a 150 µm condenser aperture and spot size 1. Images were recorded at a nominal magnification of 120,000× using a Morada G3 CCD camera controlled by RADIUS software.

Cryo-EM sample preparation and data acquisition

Purified PKR was mixed with mitapivat, etavopivat, BT-119106 or SNH-119014 at a 1:20 protein-to-ligand molar ratio and incubated at 4 °C for 2 h, and the apo-PKR control received an equal volume of DMSO, with the final DMSO concentration kept below 0.1% (v/v) in all samples. Samples were cleared by centrifugation at 12,000 r.p.m. and 4 °C for 5 min before vitrification. A total volume of 3.0 µl of each supernatant was applied to a glow-discharged (45 s, PELCO easiGlow) 200-mesh Quantifoil R1.2/1.3 Cu holey-carbon grid overlaid with a 2-nm continuous carbon film. The grid was blotted for 3 s at 100% humidity and 4 °C and plunge-frozen in liquid ethane using a Vitrobot Mark IV (Thermo Fisher Scientific), and vitrified grids were stored in liquid nitrogen until data collection.

Cryo-EM datasets were collected on a Titan Krios G3 (Thermo Fisher Scientific) operated at 300 kV and equipped with a Gatan K2 Summit direct electron detector and a BioQuantum energy filter with a 20 eV slit, using a 50 µm C2 aperture and spot size 6, at a nominal magnification of 165,000× corresponding to a calibrated pixel size of 0.85 Å, with total exposures of 53.6-59.9 e-/Å2 fractionated into 30 frames over a 6 s exposure and a defocus range of -0.8 to -1.8 µm (Table 1). Movies were acquired automatically in counting mode using EPU, yielding 4,218, 5,951, 4,317,

Langtaosha (LTS) Preprint doi: https://doi.org/10.65215/LTSpreprints.2026.11.23.000399. This version posted November 23, 2026. The copyright holder for this preprint (which was not certified by peer review) is the author/funder. Creative Commons license: CC Attribution-NonCommercial-NoDerivatives 4.0 https://creativecommons.org/licenses/by-nc-nd/4.0

3,600 and 2,272 movie stacks for apo-PKR, PKR-mitapivat, PKR-etavopivat, PKR-BT-119106 and PKR-SNH-119014, respectively.

Image processing and 3D reconstruction

Cryo-EM data were processed in cryoSPARC v4.4.1[23], RELION v5.0[24] and EMAN2 v2.39[25]. Unless noted otherwise, movie stacks were motion-corrected with patch motion correction and the contrast transfer function was estimated with patch CTF estimation in cryoSPARC, and micrographs with crystalline ice, strong drift or poor CTF fits were discarded. Particles were picked with templates generated from blob-picked 2D classes, extracted in 256 pixel boxes and cleaned by a further round of 2D classification. Ab initio reconstruction into six classes and heterogeneous refinement were used to isolate the major 3D class, and final maps were obtained by non-uniform refinement[26], reference-based motion correction and local refinement. Resolutions were estimated at the 0.143 FSC criterion, and maps used for display were sharpened with DeepEMhancer[27] and inspected in UCSF Chimera v1.18[28].

For apo-PKR, 1,183,727 particles from 4,172 selected micrographs were picked and extracted, and iterative 2D classification and heterogeneous refinement yielded a set of 996,489 particles that reconstructed the map at 2.34 Å resolution with D2 symmetry. 3D variability analysis was performed on the same particle set (Supplementary Movie 1)[29]. Focused 3D classification of the B domain without imposed symmetry separated three classes, and non-uniform refinement of the intermediate class containing 313,016 particles with D2 symmetry reconstructed the map at 2.48 Å resolution (Extended Data Fig. 4).

For PKR-mitapivat, 1,366,995 particles from 5,942 selected micrographs were picked and extracted, and iterative 2D classification and heterogeneous refinement yielded a set of 767,192 particles that reconstructed the map at 2.74 Å resolution in C1 and at 2.57 Å resolution after C2 local refinement (Extended Data Fig. 1d). C2 symmetry expansion of this set, followed by signal subtraction and focused 3D classification, produced six classes, of which three showed explicit ligand density and were refined to 2.9 Å resolution (Extended Data Fig. 2).

For PKR-etavopivat, movie stacks were motion-corrected with MotionCor2[30] and the contrast transfer function was estimated with CTFFIND4.1[31], and 4,310 micrographs were retained. Particles were picked in EMAN2 and then in RELION using templates from 2D classes, and 1,252,921 particles were imported into cryoSPARC after 2D classification. Two rounds of 3D classification yielded a final set of 243,647 particles that reconstructed the map at 2.81 Å resolution with C2 symmetry (Extended Data Fig. 3).

For PKR-BT-119106, 746,217 particles from 3,587 selected micrographs were picked and extracted, and heterogeneous refinement selected 382,074 particles. Focused 3D classification of

Langtaosha (LTS) Preprint doi: https://doi.org/10.65215/LTSpreprints.2026.11.23.000399. This version posted November 23, 2026. The copyright holder for this preprint (which was not certified by peer review) is the author/funder. Creative Commons license: CC Attribution-NonCommercial-NoDerivatives 4.0 https://creativecommons.org/licenses/by-nc-nd/4.0

the interfacial allosteric pocket yielded a final set of 250,727 particles that reconstructed the map at 2.87 Å resolution with C2 symmetry (Extended Data Fig. 5).

For PKR-SNH-119014, 361,027 particles from 2,250 selected micrographs were picked and extracted, and heterogeneous refinement yielded a final set of 213,857 particles that reconstructed the map at 2.77 Å resolution with C2 symmetry (Extended Data Fig. 6).

Model Building, Refinement, and Analysis

The apo-PKR model was built from the human PKR monomer (PDB 2VGB)[1], which was rigid-body fitted into the cryo-EM density and expanded to the tetramer in UCSF Chimera[28]. The model was adjusted manually in Coot v0.9.8.92 EL[32] and refined with phenix.real_space_refine in PHENIX v1.20.1[33], and manual rebuilding and real-space refinement were iterated. The refined apo-PKR model was used as the starting model for the mitapivat-, etavopivat-, BT-119106- and SNH-119014-bound complexes. Ligand restraints were generated with eLBOW[34], the protein and ligand were rigid-body fitted into each complex map, pocket side chains were adjusted in Coot, and the same Coot/PHENIX cycle was applied, leaving loops without continuous density unmodelled. The final models were validated with MolProbity[35], yielding model-to-map correlation coefficients (CCmask) of 0.81-0.84, and all refinement and validation statistics are summarized in Table 1.

Molecular dynamics simulations

All-atom molecular dynamics simulations were performed for PKR complexes containing one or two bound mitapivat molecules using Desmond in Maestro v14.5 (Schrödinger) [36] with the OPLS4 force field and explicit TIP3P water[37]. Each complex was solvated in an orthorhombic periodic box with a minimum solute-to-box distance of 10 Å, neutralized with counterions and adjusted to an ionic strength of 0.15 M with NaCl. Energy minimization was followed by sequential NVT and NPT equilibration, after which one 1-μs production trajectory was generated for each occupancy state in the NPT ensemble at 300 K and 1.01325 bar. Simulations used RESPA integration with a 2-fs time step, particle-mesh Ewald electrostatics and a 9 Å cutoff for short-range nonbonded interactions. Protein-backbone, ligand and binding-site root-mean-square deviations (RMSDs) and ligand–pocket interactions were analyzed using the Simulation Interaction Diagram module; structural inspection was performed in UCSF ChimeraX. Each occupancy state was simulated in a single trajectory to assess the stability of the observed binding modes[38].

Chemical synthesis

Unless otherwise stated, reagents and solvents were purchased from Adamas and used as received. DMF was distilled from sodium hydride under reduced pressure, and THF was dried over sodium

Langtaosha (LTS) Preprint doi: https://doi.org/10.65215/LTSpreprints.2026.11.23.000399. This version posted November 23, 2026. The copyright holder for this preprint (which was not certified by peer review) is the author/funder. Creative Commons license: CC Attribution-NonCommercial-NoDerivatives 4.0 https://creativecommons.org/licenses/by-nc-nd/4.0

metal and distilled before use. Reactions were monitored by thin-layer chromatography or LC–MS, and products were purified by silica-gel column chromatography. ^{1}H and ^{13}C NMR spectra were recorded on a Bruker Avance Neo spectrometer at 400 and 100 MHz, respectively, in DMSO-d_6. LC-MS analyses were performed on an Agilent Technologies 1260 II-G InfinityLab LC/MSD system. High-resolution mass spectra of key compounds were acquired by ESI–Orbitrap MS.

Mitapivat (AG-348) and etavopivat (FT-4202) were purchased from BirdoTech at >98% purity and used as received. The key intermediate 12 was prepared according to a previously reported procedure[22]. Target compounds were then obtained from this intermediate by N-sulfonylation, acidic deprotection and amide coupling. Selected analogues were prepared analogously from intermediates 12, 18 or 24.

For N-sulfonylation, triethylamine and the appropriate aryl or heteroaryl sulfonyl chloride were added in one portion to intermediate 12 in anhydrous THF. The mixture was stirred at room temperature for 16 h, quenched with water and extracted with ethyl acetate. The organic phase was washed with brine, dried over anhydrous Na_2SO_4 and purified by silica-gel chromatography. The protected sulfonamide was dissolved in trifluoroacetic acid and heated at 60 °C for 6 h. After concentration, the crude amine was coupled with the appropriate chiral α-aryl-β-hydroxy acid using HATU and DIPEA in DMF at room temperature for 16 h. Aqueous work-up was followed by silica-gel chromatography to afford the target compound.

BT-119106 was prepared using 4-cyanobenzenesulfonyl chloride and (S)-3-hydroxy-2-phenylpropanoic acid and was obtained as a white solid. HRMS (ESI–Orbitrap) m/z $[M+H]^+$ calcd for $C_{22}H_{22}N_3O_4S^+$, 424.1326; found, 424.1325.

SNH-119014 was prepared using pyridine-2-sulfonyl chloride and (S)-2-(2,4-difluorophenyl)-3-hydroxypropanoic acid, and was obtained as a white solid in 20% overall yield. LC–MS (ESI) m/z $[M+H]^+$, 436.1. HRMS (ESI–Orbitrap) m/z $[M+H]^+$ calcd for $C_{20}H_{20}F_2N_3O_4S^+$, 436.1137; found, 436.1137.

Pyruvate kinase activity assay

Recombinant PKR activity was measured using a fluorometric Pyruvate Kinase Assay Kit (Abcam, ab83432) in 20-µl reactions. Recombinant human PKLR (R&D Systems, 8569-PK; hereafter PKR) was diluted to 2.12 ng $µl^{-1}$ in PK Assay Buffer. In black, clear-bottom 384-well plates, 5 µl enzyme solution was mixed with 5 µl fourfold-concentrated compound solution. Final compound concentrations ranged from 1 to 3,000 nM, with DMSO maintained at 1% (v/v). After preincubation at 37 °C for 10 min, reactions were initiated with 10 µl reaction mixture containing 0.08 µl OxiRed Probe, 0.40 µl PK Substrate Mix, 0.20 µl PK Enzyme Mix (Developer Mix A) and 9.32 µl PK Assay Buffer. Fluorescence was recorded at 540 nm excitation and 590 nm emission every 30 s for 60 min using a PHERAstar FSX plate reader (BMG LABTECH). For ex vivo assays,

Langtaosha (LTS) Preprint doi: https://doi.org/10.65215/LTSpreprints.2026.11.23.000399. This version posted November 23, 2026. The copyright holder for this preprint (which was not certified by peer review) is the author/funder. Creative Commons license: CC Attribution-NonCommercial-NoDerivatives 4.0 https://creativecommons.org/licenses/by-nc-nd/4.0

fresh K_2EDTA-anticoagulated blood was obtained from healthy adult volunteers with written informed consent. The study was approved by the Ethics Committee of Chengdu Second People's Hospital (approval no. 2023577). Erythrocytes were isolated using a 70% isotonic Percoll gradient and washed with PBS and serum-free AGAM medium. Complete AGAM medium consisted of PBS supplemented with 1% D-glucose, 170 mg l^{-1} adenine, 5.25 g l^{-1} D-mannitol and 10% fetal bovine serum. Erythrocytes were incubated with compounds in 96-well plates at a final density of 1×10^7 cells ml^{-1}. Compound concentrations ranged from 1 to 3,000 nM, with DMSO maintained at 1% (v/v). After incubation at 37 °C under 5% CO_2 for 4 h, cells were collected and lysed in 90 µl erythrocyte lysis buffer (Beyotime, C3702). Clarified lysate (10 µl) was mixed with 10 µl reaction mixture, and fluorescence was recorded at 540/590 nm every 60 s for 60 min.

Reaction rates were calculated by linear regression of the linear region of each fluorescence progress curve, typically between 30 and 40 min. For each independent assay run, relative PK activity was calculated as:

$$A_{\mathrm{rel}}(\%) = 100 \times \frac{S_{\mathrm{compound}}}{\mathrm{mean}(S_{\mathrm{vehicle}})}$$

Concentration-response curves were fitted in GraphPad Prism v10.4.0 using a four-parameter variable-slope model, with $\log_{10}$[compound concentration (nM)] as X and relative PK activity as Y:

$$Y = \mathrm{Bottom} + \frac{\mathrm{Top} - \mathrm{Bottom}}{1 + 10^{[\log_{10}(\mathrm{AC_{50}/nM}) - X] \times \mathrm{HillSlope}}}$$

AC_{50} was defined as the concentration producing a response halfway between the fitted Bottom and Top plateaus, and the fitted Top was reported as E*max*. Unless otherwise indicated, Bottom, Top and HillSlope were unconstrained. Fit quality was evaluated using goodness-of-fit statistics and residual plots. All recombinant and donor-specific erythrocyte assays were performed in at least three independent assay runs. Data are presented as mean ± s.e.m. The two donor datasets were analysed separately, and repeated assays from the same donor were not considered independent donors.

Figure preparation

Structural figures, illustrations and videos were prepared using PyMOL v2.6[39], UCSF ChimeraX v1.7[40], UCSF Chimera v1.18[28], GraphPad Prism v10.4.0 and Adobe Illustrator.

Data availability

The cryo-EM maps and associated atomic coordinates of PKR have been deposited in the wwPDB OneDep System following the EMD accession codes and PDB IDs of EMD-65437 and 9VXP for apo-PKR, EMD-65893 and 9WDO for the C2-symmetrized PKR-mitapivat complex, EMD-65896 and 9WDQ, EMD-65900 and 9WDR, and EMD-65905 and 9WDT for the two single-ligand and

Langtaosha (LTS) Preprint doi: https://doi.org/10.65215/LTSpreprints.2026.11.23.000399. This version posted November 23, 2026. The copyright holder for this preprint (which was not certified by peer review) is the author/funder. Creative Commons license: CC Attribution-NonCommercial-NoDerivatives 4.0 https://creativecommons.org/licenses/by-nc-nd/4.0

the dual-ligand PKR-mitapivat states, EMD-65737 and 9W81 for PKR-etavopivat, EMD-65736 and 9W7Y for PKR-BT-119106, and EMD-65641 and 9W4Q for PKR-SNH-119014.

Acknowledgements

Cryo-EM data were collected on the Can Cong microscope at the SKLB West China Cryo-EM Center and processed at the SKLB Duyu High Performance Computing Center of West China Hospital. This work was supported by the university-enterprise cooperation science and technology project between Sichuan University and ScinnoHub Pharmaceutical (Chengdu) Co., Ltd (Grant No. 23H01789).

Author contributions

Z.S. conceived and supervised the project, and reviewed and edited the manuscript. H.M. performed the structural biology studies, including plasmid construction, protein expression and purification, negative-stain EM, cryo-EM sample preparation, grid screening, and data collection. H.M. also conducted the structure determination, model building, and structural analysis, and wrote the original draft of the manuscript. H.M. and Q.Y. performed the molecular dynamics simulations. J.W. and J.T. designed the target compounds, and Z.W. carried out their chemical synthesis. The PKR activity assays were conducted by L.Z. and X.H. J.T. supervised the project, secured funding, and reviewed and edited the manuscript. All authors contributed to the preparation of the manuscript and have read and approved the final version.

Competing interests

Z.W., J.W., L.Z., X.H. and J.T. are employees of ScinnoHub Pharmaceutical Co., Ltd. ScinnoHub Pharmaceutical holds patent rights and potential commercial interests in the compounds described in this study. All other authors declare no competing interests.

Langtaosha (LTS) Preprint doi: https://doi.org/10.65215/LTSpreprints.2026.11.23.000399. This version posted November 23, 2026. The copyright holder for this preprint (which was not certified by peer review) is the author/funder. Creative Commons license: CC Attribution-NonCommercial-NoDerivatives 4.0 https://creativecommons.org/licenses/by-nc-nd/4.0

Main figures

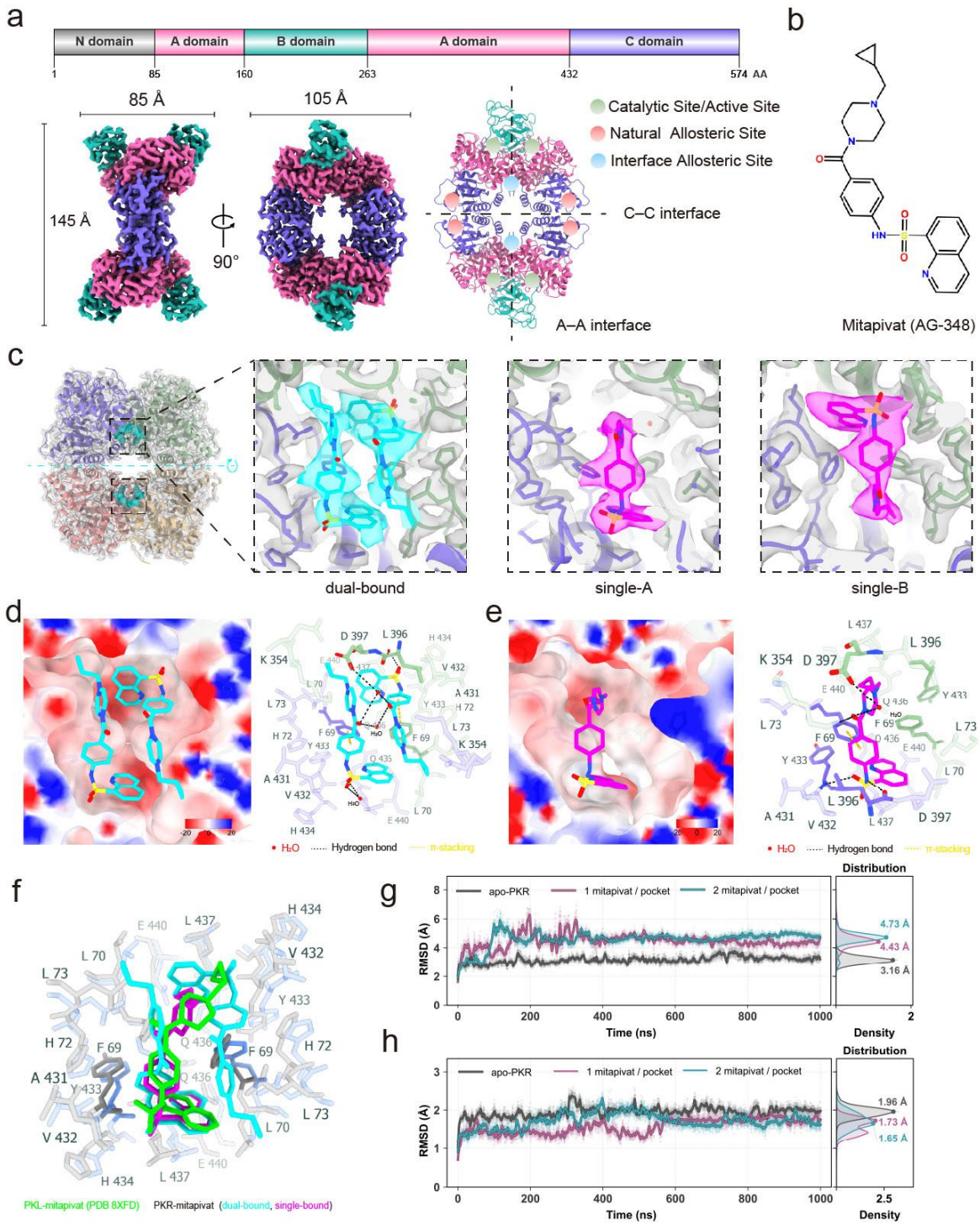


Figure 1. Mitapivat adopts single- and dual-ligand states in the PKR interfacial allosteric pocket. a, Domain organization and cryo-EM structure of the apo-PKR tetramer. N, residues 1-84; A, 85-159 and 263-431; B, 160-262; C, 432-574. b, Chemical structure of mitapivat (AG-348). c, Cryo-EM densities of the C2-symmetrized PKR-mitapivat reconstruction and of the dual-ligand and two single-ligand states separated by focused classification. d, The dual-ligand state, with two

Langtaosha (LTS) Preprint doi: https://doi.org/10.65215/LTSpreprints.2026.11.23.000399. This version posted November 23, 2026. The copyright holder for this preprint (which was not certified by peer review) is the author/funder. Creative Commons license: CC Attribution-NonCommercial-NoDerivatives 4.0 https://creativecommons.org/licenses/by-nc-nd/4.0

mitapivat molecules packed head-to-tail surrounding the A-A′ interfacial pocket. e, A representative single-ligand state. f, Superposition of mitapivat molecules in PKR single- and dual-ligand states with the mitapivat-bound PKL structure (PDB 8XFD, green). g,h, Backbone RMSD of the two pocket-forming protomers (g) and a common set of residues lining the interfacial allosteric pocket (h) in 1 μs MD simulations of apo-PKR and PKR with one or two mitapivat molecules per A-A′ pocket. Electrostatic potential surfaces are colored from negative (red) to positive (blue), red spheres indicate ordered waters, black and yellow dashed lines indicate hydrogen bonds and π-stacking interactions, respectively. RMSDs were calculated relative to the first frame of each trajectory after alignment on the backbone of the two pocket-forming protomers; faint points and solid lines show individual frames and 81-frame moving averages, respectively.

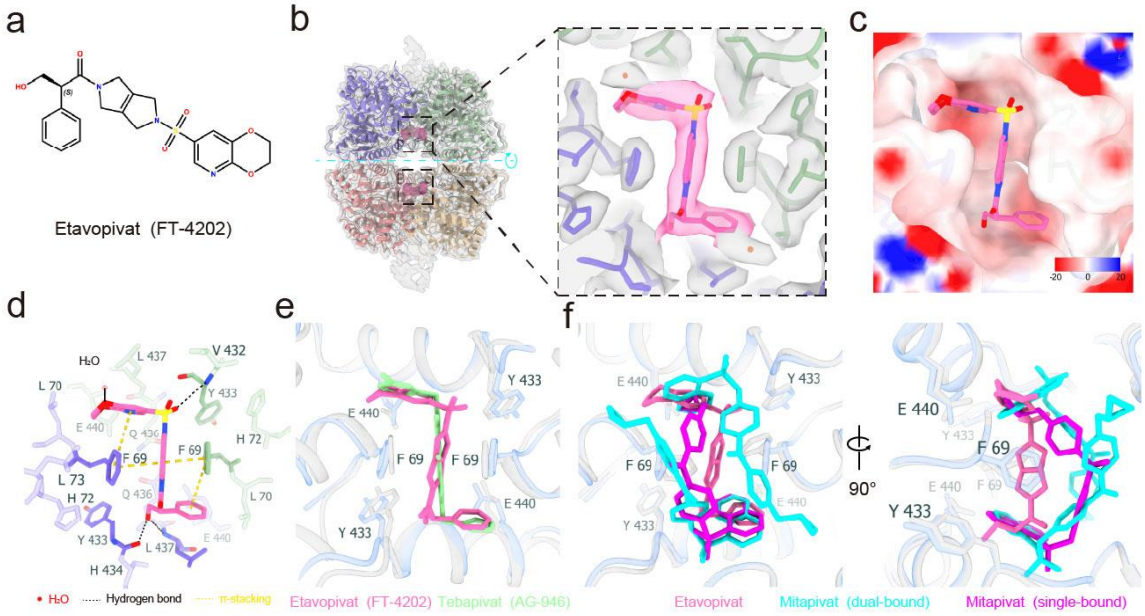


Figure 2. Etavopivat inserts into the A-A′ interfacial pocket. a, Chemical structure of etavopivat (FT-4202). b, Cryo-EM density map and atomic model of the PKR-etavopivat complex, with one etavopivat molecule in each of the two A-A′ interfacial pockets. c, Electrostatic potential surface of the etavopivat-bound pocket. d, Interaction network of etavopivat. e, Superposition with PKR-bound tebapivat (AG-946, green; PDB 8TBS). f, Superposition with the mitapivat single-ligand (magenta) and dual-ligand (cyan) states from Figure 1, shown in two views. Electrostatic potential surfaces are colored from negative (red) to positive (blue), the red sphere indicates an ordered water, and black and yellow dashed lines indicate hydrogen bonds and π-stacking interactions, respectively.

Langtaosha (LTS) Preprint doi: https://doi.org/10.65215/LTSpreprints.2026.11.23.000399. This version posted November 23, 2026. The copyright holder for this preprint (which was not certified by peer review) is the author/funder. Creative Commons license: CC Attribution-NonCommercial-NoDerivatives 4.0 https://creativecommons.org/licenses/by-nc-nd/4.0

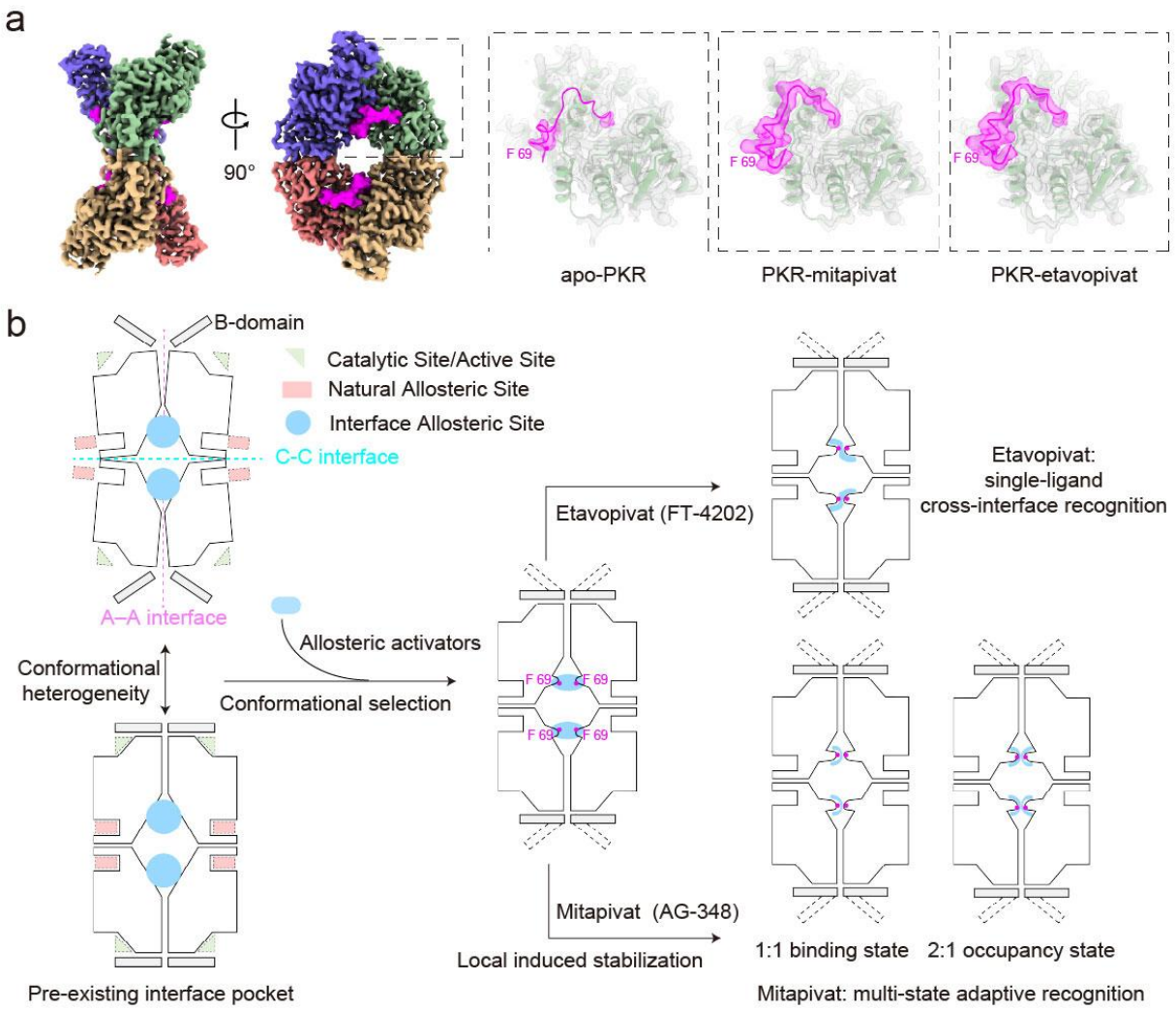


Figure 3. Agonist binding orders the regions surrounding a pre-existing allosteric pocket. a, Structural comparison of apo-PKR with the mitapivat- and etavopivat-bound complexes. The F69-containing N-terminal region bordering the A-A′ interfacial pocket is highlighted in magenta and is better resolved in both ligand-bound structures. b, Working model in which apo-PKR samples pre-existing conformations of the interfacial pocket, an agonist selects a chemically compatible conformation, and the surrounding regions are stabilized upon binding. Etavopivat adopts a single-ligand insertion pose, whereas mitapivat adopts states containing one or two ligands per pocket. The catalytic, endogenous allosteric and interfacial allosteric sites are colored green, pink and blue, respectively, and dashed outlines denote conformational heterogeneity.

Langtaosha (LTS) Preprint doi: https://doi.org/10.65215/LTSpreprints.2026.11.23.000399. This version posted November 23, 2026. The copyright holder for this preprint (which was not certified by peer review) is the author/funder. Creative Commons license: CC Attribution-NonCommercial-NoDerivatives 4.0 https://creativecommons.org/licenses/by-nc-nd/4.0

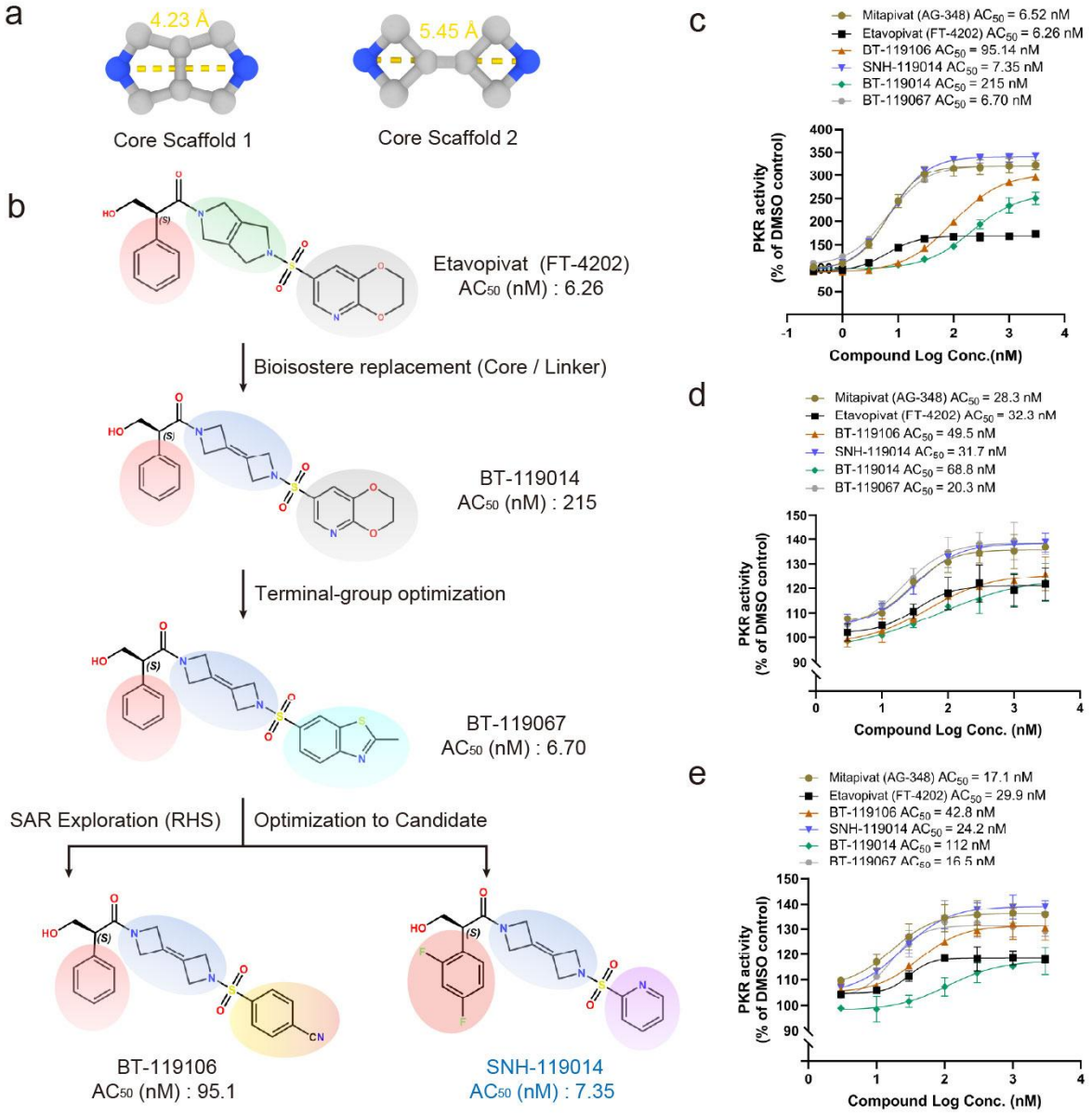


Figure 4. Pharmacophore optimization guided by the etavopivat MOA yields the clinical candidate SNH-119014. a, Comparison of the fused bicyclic diamine core of etavopivat (Core Scaffold 1) and the alkene-linked bis-azetidine core (Core Scaffold 2), with nitrogen-nitrogen distances of 4.23 and 5.45 Å, respectively. b, Optimization pathway from etavopivat through core replacement to BT-119014, terminal-group redesign to BT-119067, and further optimization of both termini to BT-119106 and SNH-119014. Shaded regions indicate the modified structural elements. c, Concentration-response curves for activation of recombinant human PKR. d-e, PK activity in erythrocyte lysates after 4 h of compound treatment of cells from a healthy male donor (d) and a healthy female donor (e). AC_{50} values determined against recombinant human PKR are

Langtaosha (LTS) Preprint doi: https://doi.org/10.65215/LTSpreprints.2026.11.23.000399. This version posted November 23, 2026. The copyright holder for this preprint (which was not certified by peer review) is the author/funder. Creative Commons license: CC Attribution-NonCommercial-NoDerivatives 4.0 https://creativecommons.org/licenses/by-nc-nd/4.0

indicated in b, and those determined in erythrocyte lysates are indicated in d and e. Activity was normalized to the 1% DMSO vehicle control and curves were fitted with a four-parameter variable-slope model. All data are presented as mean ± s.e.m. from at least three independent experiments, and the two donor samples were measured separately.

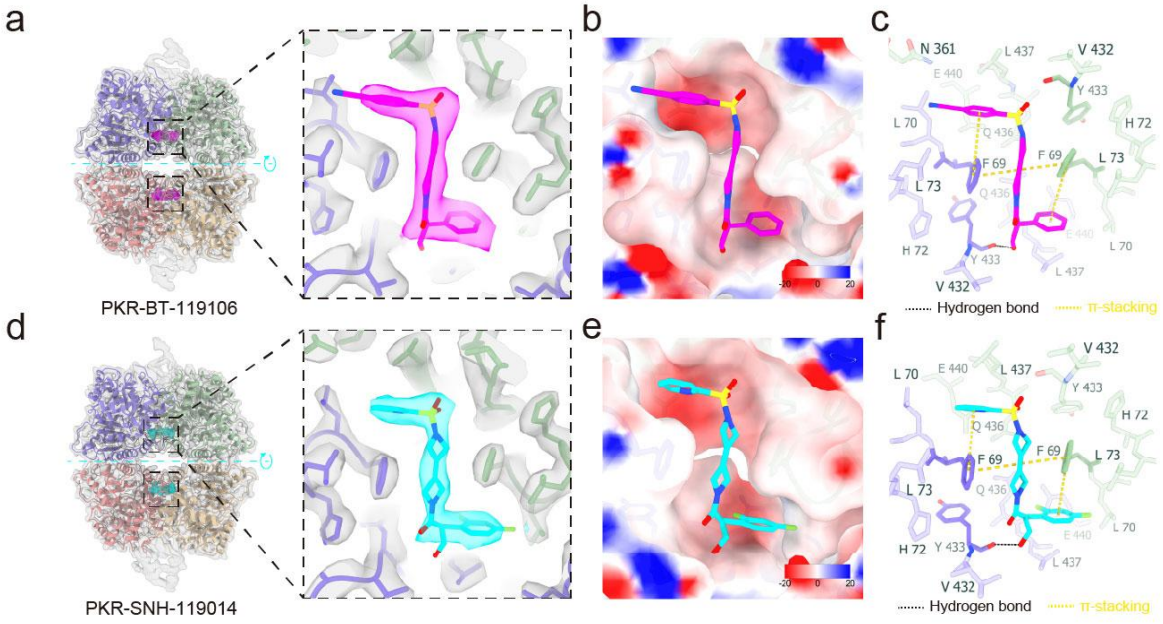


Figure 5. BT-119106 and SNH-119014 retain the etavopivat MOA. a, Cryo-EM density map and atomic model of the PKR-BT-119106 tetramer, with ligand density in the two A-A′ interfacial pockets. b, Electrostatic potential surface of the BT-119106-bound pocket. c, Local contacts of BT-119106 in the pocket. d, Cryo-EM density map and atomic model of the PKR-SNH-119014 tetramer. e, Electrostatic potential surface of the SNH-119014-bound pocket. f, Local contacts of SNH-119014 in the pocket. Electrostatic potential surfaces are colored from negative (red) to positive (blue), and black and yellow dashed lines indicate hydrogen bonds and π-stacking interactions, respectively.

Langtaosha (LTS) Preprint doi: https://doi.org/10.65215/LTSpreprints.2026.11.23.000399. This version posted November 23, 2026. The copyright holder for this preprint (which was not certified by peer review) is the author/funder. Creative Commons license: CC Attribution-NonCommercial-NoDerivatives 4.0 https://creativecommons.org/licenses/by-nc-nd/4.0

628 **Table 1.** Cryo-EM data collection, refinement and validation statistics

	apo-PKR	PKR-mitapivat (C2, dual-ligand)	PKR-mitapivat (C1, single-ligand A)	PKR-mitapivat (C1, single-ligand B)	PKR-mitapivat (C1, dual-ligand)	PKR-etavopivat (FT-4202)	PKR-BT-119106	PKR-SNH-119014
EMDB ID	65437	65893	65896	65900	65905	65737	65736	65641
PDB ID	9VXP	9WDO	9WDQ	9WDR	9WDT	9W81	9W7Y	9W4Q
Data collection and processing								
Magnification	165,000							
Voltage (kV)	300							
Electron exposure (e^{-}/Å^2)	53.6	56.1	56.1	56.1	56.1	59.9	56.2	57.8
Defocus range (μm)	-0.8 to -1.8							
Pixel size (Å)	0.85	0.85	0.85	0.85	0.85	0.85	0.85	0.85
Symmetry imposed	D2	C2	C1	C1	C1	C2	C2	C2
Initial particle images (no.)	2,153,305	3,302,349	1,534,384	1,534,384	1,534,384	2,018,940	1,550,897	953,707
Final particle images (no.)	313,016	767,192	259,335	260,529	255,694	243,647	250,727	213,857
Map resolution (Å)	2.48	2.57	2.93	2.92	2.93	2.81	2.87	2.77
FSC threshold	0.143	0.143	0.143	0.143	0.143	0.143	0.143	0.143
Map resolution range (Å)	2.3-3.9	2.3-4.1	2.3-4.9	2.3-4.7	2.6-5.0	2.5-5.9	2.4-5.3	2.5-5.3
Refinement								
Initial model used (PDB code)	2VGB				9VXP			
Model resolution (Å)	2.7	2.9	3.1	3.1	3.2	3.0	3.1	2.9
FSC threshold	0.5	0.5	0.5	0.5	0.5	0.5	0.5	0.5
Map sharpening *B* factor (Å^2)	-106.5	-140.9	-137.2	-136.9	-136.9	-116.1	-125.1	-113.6
Model composition								
Non-hydrogen atoms	15348	12868	6400	6400	6434	12860	12852	12852
Protein residues	2028	1680	840	840	840	1680	1680	1680
Nucleotides	N/A	N/A	N/A	N/A	N/A	N/A	N/A	N/A
Ligands	N/A	4	1	1	2	2	2	2
B factors (Å^2, mean)								
Protein	60.73	62.93	63.84	51.93	61.05	66.90	71.27	62.61
Nucleotide	N/A	N/A	N/A	N/A	N/A	N/A	N/A	N/A
Ligand	N/A	79.54	35.13	35.60	76.04	85.42	78.69	69.21
Root mean square deviation								
Bond lengths (Å)	0.003	0.004	0.003	0.003	0.003	0.004	0.004	0.004
Bond angles (°)	0.590	0.715	0.703	0.690	0.751	0.774	0.762	0.701
Validation								
MolProbity score	1.16	1.33	1.27	1.28	1.20	1.25	1.27	1.08
Clashscore	2.32	2.98	2.88	2.56	2.56	3.33	3.64	2.87
Poor rotamers (%)	0	0	0	0	0	0	0	0
Cross-correlation mask	0.81	0.82	0.83	0.84	0.83	0.81	0.81	0.83
Ramachandran plot								
Favored (%)	97.18	96.33	96.88	96.39	97.12	97.36	97.42	98.26
Allowed (%)	2.82	3.67	3.12	3.61	2.88	2.64	2.58	1.74
Disallowed (%)	0	0	0	0	0	0	0	0

629

630

Langtaosha (LTS) Preprint doi: https://doi.org/10.65215/LTSpreprints.2026.11.23.000399. This version posted November 23, 2026. The copyright holder for this preprint (which was not certified by peer review) is the author/funder. Creative Commons license: CC Attribution-NonCommercial-NoDerivatives 4.0 https://creativecommons.org/licenses/by-nc-nd/4.0

References

1. Valentini, G. *et al.* Structure and Function of Human Erythrocyte Pyruvate Kinase. *Journal of Biological Chemistry* **277**, 23807–23814 (2002).
2. Christofk, H. R. *et al.* The M2 splice isoform of pyruvate kinase is important for cancer metabolism and tumour growth. *Nature* **452**, 230–233 (2008).
3. Van Wijk, R. & Van Solinge, W. W. The energy-less red blood cell is lost: erythrocyte enzyme abnormalities of glycolysis. *Blood* **106**, 4034–4042 (2005).
4. Le, K. *et al.* Activating pyruvate kinase improves red blood cell integrity by reducing band 3 tyrosine phosphorylation. *Blood Advances* **8**, 5653–5662 (2024).
5. Rab, M. A. E. *et al.* Decreased activity and stability of pyruvate kinase in sickle cell disease: a novel target for mitapivat therapy. *Blood* **137**, 2997–3001 (2021).
6. Matte, A. *et al.* The pyruvate kinase activator mitapivat reduces hemolysis and improves anemia in a β-thalassemia mouse model. *Journal of Clinical Investigation* **131**, e144206 (2021).
7. Al-Samkari, H. *et al.* Diagnosis and management of pyruvate kinase deficiency: international expert guidelines. *The Lancet Haematology* **11**, e228–e239 (2024).
8. U.S. Food and Drug Administration. FDA approves treatment for anemia in adults with rare inherited disorder. https://www.fda.gov/drugs/news-events-human-drugs/fda-approves-treatment-anemia-adults-rare-inherited-disorder (2022).
9. Grace, R. F. *et al.* Safety and Efficacy of Mitapivat in Pyruvate Kinase Deficiency. *N Engl J Med* **381**, 933–944 (2019).
10. Al-Samkari, H. *et al.* Mitapivat versus Placebo for Pyruvate Kinase Deficiency. *N Engl J Med* **386**, 1432–1442 (2022).
11. Schroeder, P. *et al.* Etavopivat, a Pyruvate Kinase Activator in Red Blood Cells, for the Treatment of Sickle Cell Disease. *The Journal of Pharmacology and Experimental Therapeutics* **380**, 210–219 (2022).
12. Saraf, S. L. *et al.* Multicenter, phase 1 study of etavopivat (FT-4202) treatment for up to 12 weeks in patients with sickle cell disease. *Blood Advances* **8**, 4459–4475 (2024).
13. Liu, T. *et al.* Structure-Based Design of AG-946, a Pyruvate Kinase Activator. *ChemMedChem* **19**, e202300559 (2024).
14. Kung, C. *et al.* AG-348 enhances pyruvate kinase activity in red blood cells from patients with pyruvate kinase deficiency. *Blood* **130**, 1347–1356 (2017).
15. Ericsson, A. *et al.* FT-4202, a selective pyruvate kinase R activator for sickle cell disease. *Experimental Hematology* **141**, 104673 (2025).
16. Han, X. *et al.* High Resolution Crystal Structure of the Pyruvate Kinase Tetramer in Complex with the Allosteric Activator Mitapivat/AG-348. *Crystals* **14**, 441 (2024).
17. ScinnoHub Pharmaceutical Co., Ltd. A phase 2 study to determine the safety, efficacy, pharmacokinetics, and pharmacodynamics of SNH-119014 in adult subjects with non-transfusion-dependent thalassemia. https://clinicaltrials.gov/study/NCT07579949 (2026).

Langtaosha (LTS) Preprint doi: https://doi.org/10.65215/LTSpreprints.2026.11.23.000399. This version posted November 23, 2026. The copyright holder for this preprint (which was not certified by peer review) is the author/funder. Creative Commons license: CC Attribution-NonCommercial-NoDerivatives 4.0 https://creativecommons.org/licenses/by-nc-nd/4.0

18. Monod, J., Wyman, J. & Changeux, J.-P. On the nature of allosteric transitions: A plausible model. *Journal of Molecular Biology* **12**, 88–118 (1965).
19. Koshland, D. E., Némethy, G. & Filmer, D. Comparison of Experimental Binding Data and Theoretical Models in Proteins Containing Subunits. *Biochemistry* **5**, 365–385 (1966).
20. Henzler-Wildman, K. & Kern, D. Dynamic personalities of proteins. *Nature* **450**, 964–972 (2007).
21. Stenström, O., Diehl, C., Modig, K. & Akke, M. Ligand-induced protein transition state stabilization switches the binding pathway from conformational selection to induced fit. *Proc. Natl. Acad. Sci. U.S.A.* **121**, e2317747121 (2024).
22. Zhao, S. *et al.* Double-bonded azacycles used as bioisosteric moieties in drug discovery. *Tetrahedron Letters* **129**, 154719 (2023).
23. Punjani, A., Rubinstein, J. L., Fleet, D. J. & Brubaker, M. A. cryoSPARC: algorithms for rapid unsupervised cryo-EM structure determination. *Nat Methods* **14**, 290–296 (2017).
24. Scheres, S. H. W. RELION: Implementation of a Bayesian approach to cryo-EM structure determination. *Journal of Structural Biology* **180**, 519–530 (2012).
25. Tang, G. *et al.* EMAN2: An extensible image processing suite for electron microscopy. *Journal of Structural Biology* **157**, 38–46 (2007).
26. Punjani, A., Zhang, H. & Fleet, D. J. Non-uniform refinement: Adaptive regularization improves single-particle cryo-EM reconstruction. *Nat Methods* **17**, 1214–1221 (2020).
27. Sanchez-Garcia, R. *et al.* DeepEMhancer: a deep learning solution for cryo-EM volume post-processing. *Commun Biol* **4**, 874 (2021).
28. Pettersen, E. F. *et al.* UCSF Chimera—A visualization system for exploratory research and analysis. *J Comput Chem* **25**, 1605–1612 (2004).
29. Punjani, A. & Fleet, D. J. 3D variability analysis: Resolving continuous flexibility and discrete heterogeneity from single particle cryo-EM. *Journal of Structural Biology* **213**, 107702 (2021).
30. Zheng, S. Q. *et al.* MotionCor2: anisotropic correction of beam-induced motion for improved cryo-electron microscopy. *Nat Methods* **14**, 331–332 (2017).
31. Rohou, A. & Grigorieff, N. CTFFIND4: Fast and accurate defocus estimation from electron micrographs. *Journal of Structural Biology* **192**, 216–221 (2015).
32. Emsley, P., Lohkamp, B., Scott, W. G. & Cowtan, K. Features and development of *Coot*. *Acta Crystallogr D Biol Crystallogr* **66**, 486–501 (2010).
33. Afonine, P. V. *et al.* Real-space refinement in *PHENIX* for cryo-EM and crystallography. *Acta Crystallogr D Struct Biol* **74**, 531–544 (2018).
34. Liebschner, D. *et al.* Macromolecular structure determination using X-rays, neutrons and electrons: recent developments in *Phenix*. *Acta Crystallogr D Struct Biol* **75**, 861–877 (2019).
35. Williams, C. J. *et al.* MolProbity: More and better reference data for improved all-atom structure validation. *Protein Science* **27**, 293–315 (2018).

Langtaosha (LTS) Preprint doi: https://doi.org/10.65215/LTSpreprints.2026.11.23.000399. This version posted November 23, 2026. The copyright holder for this preprint (which was not certified by peer review) is the author/funder. Creative Commons license: CC Attribution-NonCommercial-NoDerivatives 4.0 https://creativecommons.org/licenses/by-nc-nd/4.0

36. Bowers, K. J. et al. Scalable algorithms for molecular dynamics simulations on commodity clusters. in Proceedings of the 2006 ACM/IEEE Conference on Supercomputing, Article 84 (ACM, 2006).
37. Lu, C. *et al.* OPLS4: Improving Force Field Accuracy on Challenging Regimes of Chemical Space. *J. Chem. Theory Comput.* **17**, 4291–4300 (2021).
38. Knapp, B., Ospina, L. & Deane, C. M. Avoiding False Positive Conclusions in Molecular Simulation:The Importance of Replicas. *Journal of Chemical Theory and Computation* **14**, 6127–6138 (2018).
39. Schrödinger, LLC. The PyMOL Molecular Graphics System, Version 2.6. https://pymol.org/.
40. Pettersen, E. F. *et al.* UCSF ChimeraX: Structure visualization for researchers, educators, and developers. *Protein Science* **30**, 70–82 (2021).